Bulletin of the Seismological Society of America, Vol. 102, No. 4, pp. 1829–1849, August 2012, doi: 10.1785/0120110272

Deep-Focus Repeating Earthquakes in the Tonga–Fiji Subduction Zone

by Wen-che Yu and Lianxing Wen*

Abstract Deep-focus earthquakes in the Tonga–Fiji subduction zone make up greater than 66% of the globally recorded deep seismicity. The high number of deep-focus seismicity in this active subduction zone allows us to search for deep-focus similar earthquake pairs and repeating earthquakes. We compile a waveform dataset for deep earthquakes with magnitude above 4.7 occurring in the Tonga–Fiji–Kermadec subduction zone recorded teleseismically between 1990 and 2009. We identify 8 similar clusters and 18 similar doublets with an average cross-correlation coefficient greater than 0.8 among more than 45,000 potential earthquake pairs. These similar doublets and clusters are located in the central part of the Tonga–Fiji slab at the depth range of 480–650 km. A master event relocation algorithm is used to determine the precise relative location and depth among these similar earthquake pairs. We estimate and superpose circular fault areas for these similar clusters and doublets and find that one similar doublet appears to be a deep repeating earthquake pair. This deep doublet has a small separation less than 0.4 km and overlapping rupture areas, indicating that the same fault appears to slip. Other deep similar earthquake pairs are spatially offset or do not exhibit overlapping rupture areas. Time separation is on the order of years for the majority of similar earthquake pairs. Thermal (plastic) shear instability is more likely to explain these deep repeating earthquakes and similar earthquake pairs.

Introduction

Earthquakes occurring below 60 km depth are confined to the inclined planar regions of the subducting slab termed Wadati–Benioff zones. Intermediate-focus (depth range of 60–300 km) and deep-focus (depth range of 300–660 km) earthquakes are unexpected, because the slab should have already passed through the brittle-ductile transition. As pressure and temperature increase with depth, high normal stresses should inhibit fracture and frictional sliding and the material should deform by ductile flow. Models proposed to explain the physical mechanisms of intermediate- and deep-focus earthquakes include dehydration embrittlement (Meade and Jeanloz, 1991; Jung *et al.*, 2004; Zhang *et al.*, 2004), thermal and plastic shear instability (Ogawa, 1987; Hobbs and Ord, 1988; Kanamori *et al.*, 1998; Karato *et al.*, 2001; Weidner *et al.*, 2001; Wiens and Snider, 2001), and shear instability induced by phase transformational faulting (Green and Burnley, 1989; Green *et al.*, 1990; Kirby *et al.*, 1996). Recent deformation experiments applicable to intermediate depths showed that dehydration of antigorite serpentinite produces faults delineated by superplastic, very fine-grained aggregates (Jung *et al.*, 2004). Others have proposed that intermediate and deep earthquakes occur due to activation of thermal shear instability that lowers viscosity and promotes a positive feedback process in which further slip and heat are generated (Ogawa, 1987; Kanamori *et al.*, 1998; Karato *et al.*, 2001; Wiens and Snider, 2001). The plastic shear instability model differs from the thermal shear instability model in that the interplay between strain rate hardening (softening) and stress relaxation can account for the occurrence of earthquakes in the transition zone and cessation of seismicity in the lower mantle (Hobbs and Ord, 1988; Weidner *et al.*, 2001; Wiens, 2001). To explain deep earthquakes, the phase transformational faulting model predicts that superplastic, very fine-grained anticracks are formed at a narrow pressure range of 1–2 GPa and a temperature interval of 1100°–1200° K during the phase transition from metastable olivine to a spinel structure. The propagation and linking-up of spinel-filled anticracks can account for the double-couple component of deep earthquakes (Green and Burnley, 1989). The phase transformational faulting model implies formation of new faults and predicts no deep repeating earthquakes. The thermal (plastic) shear instability model bears no assumption on the formation of faults and more likely accounts for the occurrence of deep repeating earthquakes.

Subduction zone seismicity is characterized by a bimodal depth distribution: a high level of seismicity in the uppermost 60 km, followed by an exponential decrease below 60 km down to 400 km depth, with another increase occurring in the transition zone (in the depth range of 410–660 km),

*Also at School of Earth and Space Sciences, University of Science and Technology of China, Hefei, Anhui 230026, China.

and abrupt cessation in the lower mantle (Frohlich, 1989). Hypocentral locations refine the morphology of the downgoing slab (Hasegawa *et al.*, 1978; Kawakatsu, 1985; Engdahl *et al.*, 1998; Chen and Brudzinski, 2001; Frohlich, 2006), and focal mechanisms constrain the state of stress and strain rate in the slab (Isacks and Molnar, 1969, 1971; Giardini and Woodhouse, 1984; Kawakatsu, 1985; Giardini and Woodhouse, 1986; Holt, 1995; Christova and Scholz, 2003). The large 1994 Tonga deep earthquake (M_w 7.6, 564 km depth) and the 1994 Bolivia deep earthquake (M_w 8.3, 636 km depth) provide a cornerstone for our understanding of source processes and mechanisms of deep earthquakes. The rupture dimensions of these large deep earthquakes can be inferred from the spatial extent of early aftershocks (Wiens *et al.*, 1994; Myers *et al.*, 1995; Wiens and McGuire, 2000) and waveform directivity (Kikuchi and Kanamori, 1994; Beck *et al.*, 1995; Chen, 1995; Silver *et al.*, 1995; Chen *et al.*, 1996; McGuire *et al.*, 1997). The 1994 Tonga deep earthquake had an extensive aftershock sequence compared with previous large deep earthquakes (Frohlich, 1987; Willemann and Frohlich, 1987; Wiens *et al.*, 1994). The moment release of the 1994 Tonga deep earthquake was mainly along a near-vertical nodal plane (Wiens *et al.*, 1994). The 1994 Bolivia deep earthquake was characterized by at least four subevents, significant moment release along a near-horizontal nodal plane, and relatively low aftershock activities. Moreover, the slow rupture velocity, high stress drop, and low seismic efficiency of the Bolivia event suggested that frictional melting likely promoted fault slip (Kanamori *et al.*, 1998). Seismological properties and physical models of intermediate and deep earthquakes are discussed in detail in several review papers (Frohlich, 1989; Green and Houston, 1995; Kirby *et al.*, 1996; Karato *et al.*, 2001; Wiens, 2001; Houston, 2007) and the book *Deep Earthquakes* (Frohlich, 2006).

Seismically inferred source parameters can be used to assess the physical models of deep earthquakes. Rupture dimensions of large deep earthquakes have been shown to be wider than the estimated dimensions of the metastable olivine wedge, essential for the initiation of phase transformational faulting (Wiens *et al.*, 1994; Beck *et al.*, 1995; Chen, 1995; Silver *et al.*, 1995; McGuire *et al.*, 1997). This indicates that transformational faulting may initiate rupture inside the metastable olivine wedge, but thermal (plastic) shear instability is likely responsible for the continuation of rupture in the spinel regime. Identifying nodal planes for large intermediate and deep earthquakes can address whether intermediate and deep earthquakes are reactivated from the preexisting weak zones (Jiao *et al.*, 2000; Warren and Silver, 2006; Warren *et al.*, 2007; Warren *et al.*, 2008). Identification of nodal planes reveals that intermediate earthquakes exhibit subhorizontal fault planes and oceanward rupture propagation, orientations that are inconsistent with the preexisting subvertical normal fault planes created in the outer-rise after correction of the subduction angle. This inconsistency suggests that new faults are created at intermediate depth (Warren *et al.*, 2007; Warren *et al.*, 2008). For deep earthquakes occurring in the depth range of 300–600 km, the nodal planes are either subvertical or subhorizontal, indicating both reactivation of the preexisting weak zones and creation of new faults. Deep earthquakes occurring close to the bottom of the transition zone exhibit subhorizontal nodal planes that may indicate formation of new faults and support the transformational faulting model (Warren *et al.*, 2007). In addition, the discovery of deep repeating earthquakes would be incompatible with the transformational faulting model (Wiens and Snider, 2001).

The Tonga–Fiji subduction zone is characterized by the highest intensity of moderate size (body-wave magnitude, m_b 4–6) deep-focus earthquakes among the circum-Pacific subduction zones. The rapid convergence rate between the Pacific plate and Australian plate (~24 cm/year) resulting from the rapid back arc extension of the Lau Basin can account for the highest level of deep seismicity (Bevis *et al.*, 1995). Previous seismic studies reported deep repeating earthquakes and similar earthquake pairs using a temporary seismic experiment deployed in the southwest Pacific between 1993 and 1995 (Wiens *et al.*, 1994; Wiens *et al.*, 1997; Wiens and Snider, 2001). In this study, we search for similar deep earthquake pairs occurring along the Tonga–Fiji–Kermadec subduction zone recorded by the Global Seismographic Network (GSN) from 1990 to 2009. A master event relocation algorithm is applied to determine the precise relative location and depth between similar earthquake pairs. We then estimate the rupture areas of earthquakes by assuming a Brune source model. This allows us to address whether the earthquakes have overlaying rupture areas and identify possible deep repeating earthquakes. The physical models of deep earthquakes are discussed in the context of repeating earthquakes and similar earthquake pairs. The term "repeating earthquakes" is hereafter defined as events where the fault areas overlie one another, whereas the term "similar earthquake pairs" describes events whose waveforms are highly correlated but do not have overlapping rupture zones. We will demonstrate that deep similar earthquake pairs are not necessarily equivalent to deep repeating earthquakes.

Searching for Deep-Focus Similar Earthquake Pairs along the Tonga–Fiji–Kermadec Subduction Zone

Spatial separation and waveform cross-correlation (cc) coefficient are used as the initial and secondary constraints to screen the potential earthquake pairs. We first divide deep events with m_b above 4.7 in the PDE catalog into a $0.5° \times 0.5°$ grid in the Tonga–Fiji–Kermadec regions (178° E–166° W and 10° S–48° S). We compute spatial separation between any two events within a grid element and in the neighboring grid elements. Events separated by less than 60 km are considered as potential event pairs. There are 2168 deep events with m_b above 4.7 in our database between 1990 and 2009; more than 45,000 potential pairs satisfy the initial spatial separation constraint. We collect seismic waveforms for each event recorded by the GSN and regional seismic networks (see Data and Resources). We band-pass filter the *P* and *PKP* waveforms in a 30-s time window in the frequency range of 0.8–2 Hz and calculate the cross-correlation (cc) coefficient for all 45,000 potential pairs. More than 6 million times of waveform cc are computed to search for deep similar earthquake pairs. We find 8 similar clusters (consisting of multiple events) and 18 similar doublets with an average cc coefficient above 0.8 in the central part of the Tonga–Fiji slab

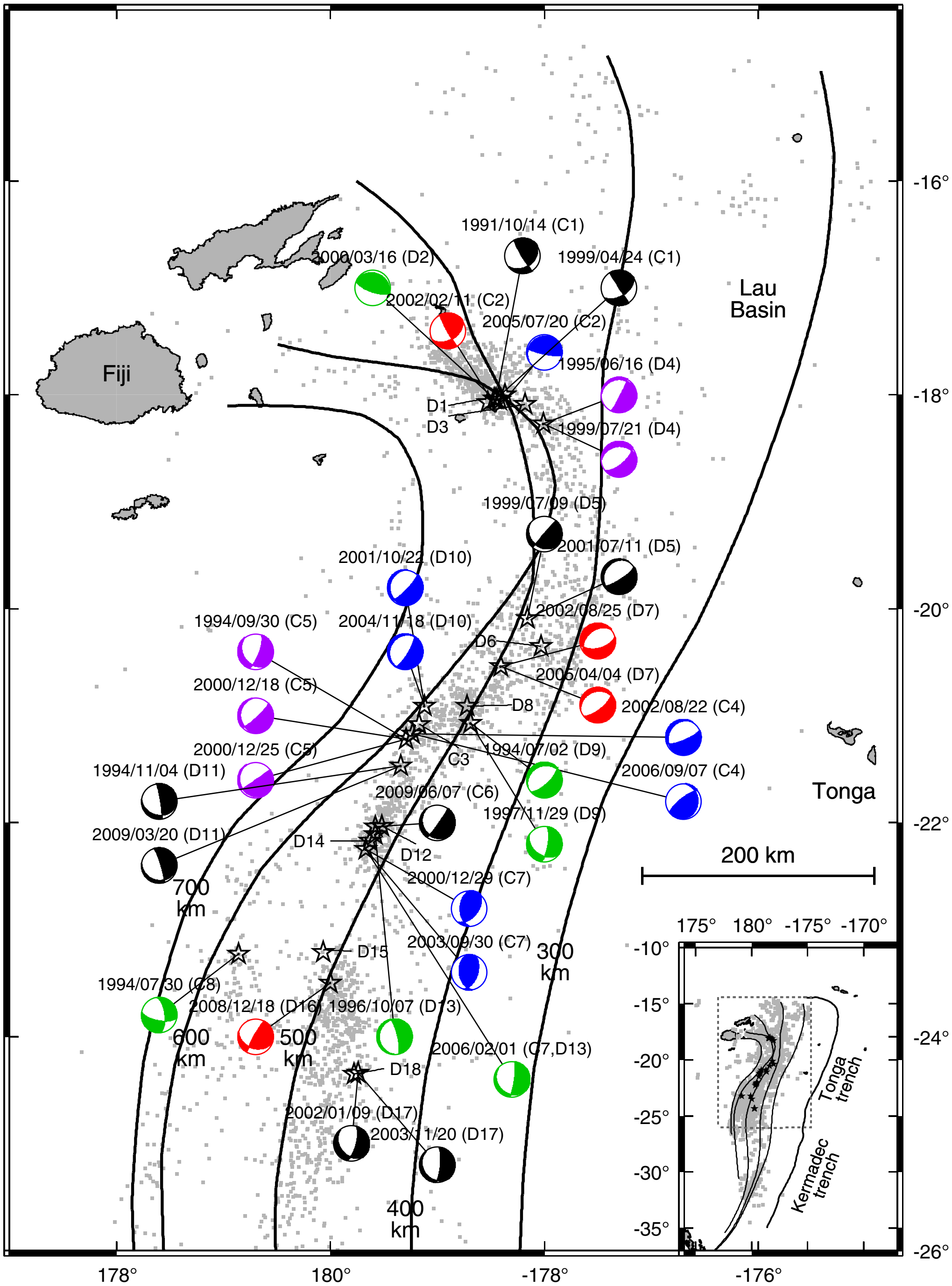

Figure 1. Regional map of deep-focus similar earthquake pairs and seismicity near the Tonga–Fiji subduction zone. Deep similar earthquake pairs (black stars) and their available Global Centroid Moment Tensor (CMT) (Dziewonski *et al.*, 1981; Ekstrom *et al.*, 2003) are labeled with event date and doublet/cluster ID where applicable. Source parameters of the doublets/clusters are listed in Tables 1, 2. Background deep seismicity is shown as gray dots. Black lines indicate the slab contours below 300 km depth (Gudmundsson and Sambridge, 1998), with an interval of 100 km. Regional map of the Tonga–Fiji–Kermadec subduction zone is shown in the inset, with gray dotted box indicating the region blow-up in the main figure. Black lines are the slab contours below 300 km depth and the Tonga–Kermadec trench (Bird, 2003). The color version of this figure is available only in the electronic edition.

Table 1
Deep-Focus Similar Doublets in the Tonga–Fiji Slab*

Origin Date (yyyy/mm/dd)	Origin Time (hh:mm:ss.ss)	Latitude (° N)	Longitude (° E)	Depth (km)	m_b †	dt (yr)‡	cc§	N_{ph}	rms‖ (ms)	dh_c # (km)	dz_c # (km)	dh_r # (km)	dz_r # (km)	$ellp_{maj}$ ** (km)	$ellp_{min}$ ** (km)
TD-D1															
1994/11/30	06:37:14.80	−18.001	−178.374	565.0	5.2	–	1.00	–	–	–	–	–	–	–	–
1996/01/08	13:40:59.24	−18.012	−178.386	567.2	4.8	1.1	0.80	18	96	13.36	32.00	1.76	2.20	14.09	6.55
TD-D2															
2000/03/16	01:42:36.44	−17.887	−178.676	630.0	4.9	–	1.00	–	–	–	–	–	–	–	–
2007/05/23	15:59:27.16	−17.891	−178.680	627.4	4.8	7.2	0.88	72	13	27.78	−57.00	0.61	−2.60	2.33	1.33
TD-D3															
1997/12/13	04:39:06.50	−18.090	−178.178	582.0	5.3	–	1.00	–	–	–	–	–	–	–	–
2002/04/10	07:11:03.79	−18.051	−178.204	599.0	4.7	4.3	0.82	32	24	9.96	18.00	5.13	17.00	4.45	3.50
TD-D4															
1995/06/16	13:49:49.30	−18.269	−178.010	566.0	5.6	–	1.00	–	–	–	–	–	–	–	–
1999/07/21	03:10:44.46	−18.193	−177.871	560.0	5.4	4.1	0.86	71	89	10.79	−6.00	16.94	−6.00	4.20	2.67
TD-D5															
1999/07/09	18:16:20.93	−20.095	−178.160	567.0	5.0	–	1.00	–	–	–	–	–	–	–	–
2001/07/11	15:11:49.79	−20.154	−178.115	553.5	5.0	2.0	0.83	75	22	20.44	−5.00	8.07	−13.50	1.42	0.77
TD-D6															
1994/09/02	17:46:16.80	−20.349	−178.028	539.0	5.0	–	1.00	–	–	–	–	–	–	–	–
1995/10/31	06:20:39.76	−20.316	−178.032	541.6	4.8	1.2	0.83	19	9	32.73	58.00	3.69	2.60	14.96	7.23
TD-D7															
2002/08/25	04:42:11.56	−20.543	−178.409	554.0	5.4	–	1.00	–	–	–	–	–	–	–	–
2005/04/04	08:16:21.93	−20.510	−178.415	558.8	5.2	2.6	0.89	105	12	10.37	−12.00	3.72	4.80	2.57	1.22
TD-D8															
2004/07/10	16:16:32.94	−20.913	−178.722	584.0	4.7	–	1.00	–	–	–	–	–	–	–	–
2005/04/22	11:25:46.31	−20.955	−178.814	592.5	4.7	0.8	0.80	59	24	17.47	5.00	10.63	8.50	1.48	0.43
TD-D9															
1994/07/02	05:46:54.10	−21.071	−178.695	567.0	5.3	–	1.00	–	–	–	–	–	–	–	–
1997/11/29	02:42:27.34	−21.013	−178.729	584.0	5.2	3.4	0.87	44	25	8.52	14.00	7.35	17.00	7.09	6.26
TD-D10															
2001/10/22	06:46:48.07	−20.908	−179.125	622.0	5.5	–	1.00	–	–	–	–	–	–	–	–
2004/11/18	12:27:08.86	−20.928	−179.125	618.2	5.2	3.1	0.83	93	15	17.80	3.00	2.22	−3.80	1.53	1.11
TD-D11															
1994/11/04	08:27:30.60	−21.473	−179.341	616.0	5.3	–	1.00	–	–	–	–	–	–	–	–
2009/03/20	12:26:03.66	−21.470	−179.342	616.2	5.0	14.4	0.88	60	19	4.29	6.30	0.35	0.20	1.67	1.00

(*continued*)

Table 1 (*Continued*)

Origin Date (yyyy/mm/dd)	Origin Time (hh:mm:ss.ss)	Latitude (° N)	Longitude (° E)	Depth (km)	m_b†	dt (yr)‡	cc§	N_{ph}	rms‖ (ms)	dh_c# (km)	dz_c# (km)	dh_r# (km)	dz_r# (km)	$ellp_{maj}$** (km)	$ellp_{min}$** (km)
TD-D12															
1996/07/12	13:31:10.00	−22.030	−179.520	573.0	4.8	–	1.00	–	–	–	–	–	–	–	–
2003/08/20	23:54:02.01	−22.028	−179.515	572.2	4.8	7.1	0.90	23	22	16.10	18.00	0.56	−0.80	2.33	2.00
TD-D13															
1996/10/07	09:23:56.90	−22.113	−179.577	606.0	5.2	–	1.00	–	–	–	–	–	–	–	–
2006/02/01	18:28:50.80	−22.195	−179.621	587.5	5.2	9.3	0.85	67	19	11.45	−7.00	10.18	−18.50	6.76	3.34
TD-D14															
1998/01/24	17:57:54.60	−22.173	−179.628	600.0	4.7	–	1.00	–	–	–	–	–	–	–	–
2003/03/15	07:03:04.72	−22.191	−179.640	599.8	4.7	5.1	0.80	24	17	14.60	−5.00	2.35	−0.20	4.51	2.06
TD-D15															
1996/11/10	06:26:21.71	−23.212	179.925	600.0	5.1	–	1.00	–	–	–	–	–	–	–	–
1997/05/21	09:29:53.92	−23.192	179.932	604.0	4.9	0.5	0.82	14	19	13.47	−50.00	2.34	4.00	2.23	1.18
TD-D16															
2008/12/18	20:57:39.00	−23.495	−179.996	542.6	5.3	–	1.00	–	–	–	–	–	–	–	–
2004/05/22	14:33:52.19	−23.611	−180.077	538.4	5.0	−4.6	0.80	20	22	3.78	−15.60	15.31	−4.20	1.27	0.38
TD-D17															
2002/01/09	01:03:38.58	−24.338	−179.743	489.0	5.2	–	1.00	–	–	–	–	–	–	–	–
2003/11/20	02:01:24.40	−24.332	−179.749	485.0	5.4	1.9	0.86	71	20	4.51	−9.00	0.90	−4.00	1.70	1.18
TD-D18															
2004/11/06	07:04:38.48	−24.347	−179.785	497.0	4.7	–	1.00	–	–	–	–	–	–	–	–
2009/10/31	10:38:12.11	−24.327	−179.804	493.8	4.9	5.0	0.80	32	56	6.02	2.50	2.94	−3.20	1.51	1.16

*The first event for each doublet refers to the master (reference) event with origin time fixed to that of the PDE catalog. Event origin time of the second event is corrected for the origin time error between the doublet, inferred from the master event relocation.

†m_b is body-wave magnitude.

‡dt is the time separation between the master and second events in years (yr).

§cc is the average cross-correlation coefficient calculated by the number of seismic phases (N_{ph}) used for the master event relocation.

‖ rms is the root-mean-square time residual between the doublet predicted based on the optimum location and depth of the second event relative to the master event in the unit of millisecond (ms).

\# dh_c and dz_c correspond to horizontal and vertical separation between the doublet based on the PDE catalog, respectively; dh_r and dz_r indicate horizontal and vertical separation between the doublet after the master event relocation, respectively.

**$ellp_{maj}$ and $ellp_{min}$ are the major and minor axes of the 95% confidence ellipse, respectively.

Table 2
Deep-Focus Similar Clusters in the Tonga–Fiji Slab*

Origin Date (yyyy/mm/dd)	Origin Time (hh:mm:ss.ss)	Latitude (° N)	Longitude (° E)	Depth (km)	m_b	dt (yr)	cc	N_{ph}	rms (ms)	dh_c (km)	dz_c (km)	dh_r (km)	dz_r (km)	$ellp_{maj}$ (km)	$ellp_{min}$ (km)
TD-C1															
1999/04/24	08:45:16.88	−18.043	−178.449	567.0	5.2	–	1.00	–	–	–	–	–	–	–	–
1991/10/14	14:35:57.81	−18.072	−178.478	568.8	5.3	−7.5	0.82	16	108	5.66	16.00	4.45	1.80	25.87	11.02
1995/10/01	16:38:37.74	−18.011	−178.470	564.4	4.8	−3.6	0.83	24	35	16.16	20.00	4.19	−2.60	3.34	1.67
1997/02/13	12:12:34.28	−18.064	−178.370	568.2	4.7	−2.2	0.78	36	33	8.53	17.00	8.67	1.20	4.06	2.67
TD-C2															
1999/02/15	09:41:52.90	−18.065	−178.530	624.0	4.7	–	1.00	–	–	–	–	–	–	–	–
1994/11/09	14:41:39.03	−18.040	−178.536	632.4	4.9	−4.3	0.86	29	8	11.84	−34.00	2.85	8.40	9.77	2.33
2000/04/01	12:14:57.67	−18.016	−178.594	621.0	4.8	1.1	0.86	40	19	28.55	15.00	8.69	−3.00	4.45	3.34
2002/02/11	03:39:32.46	−18.079	−178.532	627.2	4.9	3.0	0.89	39	15	4.60	−33.00	1.57	3.20	5.78	2.56
2005/07/20	04:48:11.44	−18.037	−178.549	623.7	4.9	6.4	0.91	44	9	7.39	−40.00	3.70	−0.30	7.78	1.66
TD-C3															
1999/10/05	14:40:22.40	−21.084	−179.173	600.0	4.8	–	1.00	–	–	–	–	–	–	–	–
2002/06/29	11:14:01.66	−21.075	−179.156	602.8	4.9	2.7	0.81	50	21	12.41	38.00	2.03	2.80	0.91	0.47
2007/11/21	06:48:32.01	−21.085	−179.190	599.1	4.9	8.1	0.82	34	17	6.17	7.00	1.77	−0.90	2.67	1.67
TD-C4															
1997/04/10	10:43:01.90	−21.168	−179.227	624.0	4.8	–	1.00	–	–	–	–	–	–	–	–
2001/06/18	14:50:56.39	−21.138	−179.245	633.5	4.8	4.2	0.83	9	10	11.88	−24.00	3.82	9.50	13.37	4.24
2002/08/22	23:58:09.58	−21.102	−179.115	617.2	5.2	5.4	0.85	10	18	15.57	−6.00	13.74	−6.80	33.35	16.32
2006/09/07	21:23:00.12	−21.075	−179.203	617.5	5.0	9.4	0.82	15	19	16.93	−25.00	10.64	−6.50	2.51	1.20
2007/12/02	15:57:40.78	−21.187	−179.236	623.4	4.8	10.6	0.85	12	22	18.18	−22.00	2.31	−0.60	3.79	1.78
TD-C5															
1994/09/30	19:30:18.40	−21.217	−179.293	643.0	5.3	–	1.00	–	–	–	–	–	–	–	–
2000/12/18	01:19:20.14	−21.170	−179.159	642.2	6.4	6.2	0.88	63	46	18.18	−15.00	14.84	−0.80	4.53	2.20
2000/12/25	05:11:57.99	−21.183	−179.199	648.8	5.3	6.2	0.86	62	80	18.17	1.00	10.45	5.80	4.03	3.79
2006/03/03	12:54:18.21	−21.162	−179.172	649.0	4.8	11.4	0.84	46	57	30.08	−15.00	13.96	6.00	15.51	7.02
TD-C5-00a-00b															
2000/12/18	01:19:21.65	−21.178	−179.124	628.0	6.4	–	1.00	–	–	–	–	–	–	–	–
2000/12/25	05:12:00.21	−21.195	−179.152	627.1	5.3	0.0	0.91	185	13	8.90	16.00	3.46	−0.90	2.00	0.78
TD-C6															
2009/06/07	12:46:30.00	−22.037	−179.583	590.0	5.1	–	1.00	–	–	–	–	–	–	–	–
2004/01/13	09:40:33.47	−22.059	−179.585	591.6	5.0	−5.4	0.82	74	51	4.68	19.00	2.46	1.60	3.67	2.45
2008/01/15	18:00:54.02	−22.036	−179.584	587.4	5.2	−1.4	0.81	88	39	12.18	−17.20	0.15	−2.60	3.34	2.00

(*continued*)

Table 2 (*Continued*)

Origin Date (yyyy/mm/dd)	Origin Time (hh:mm:ss.ss)	Latitude (° N)	Longitude (° E)	Depth (km)	m_b	dt (yr)	cc	N_{ph}	rms (ms)	dh_c (km)	dz_c (km)	dh_r (km)	dz_r (km)	$ellp_{maj}$ (km)	$ellp_{min}$ (km)
TD-C7															
2000/12/29	23:33:53.07	−22.253	−179.672	584.0	5.1	–	1.00	–	–	–	–	–	–	–	–
1993/11/19	04:37:56.60	−22.275	−179.675	583.6	5.3	−7.1	0.89	52	19	22.99	7.00	2.47	−0.40	1.96	1.18
2003/09/30	02:01:05.11	−22.202	−179.672	586.2	5.0	2.8	0.86	88	24	2.34	4.00	5.67	2.20	3.34	2.22
2006/02/01	18:28:49.39	−22.183	−179.658	600.0	5.2	5.1	0.84	89	18	6.98	15.00	7.92	16.00	2.46	1.33
TD-C8															
1994/07/30	14:34:08.70	−23.227	179.137	545.0	5.1	–	1.00	–	–	–	–	–	–	–	–
1993/12/14	13:21:25.61	−23.266	179.073	545.0	4.8	−0.6	0.82	13	9	40.46	42.00	7.85	0.00	36.27	12.94
2006/04/08	08:04:08.88	−23.195	179.123	546.4	4.7	11.7	0.82	22	11	8.37	30.00	3.83	1.40	9.82	5.94

*Column headings are the same as Table 1.

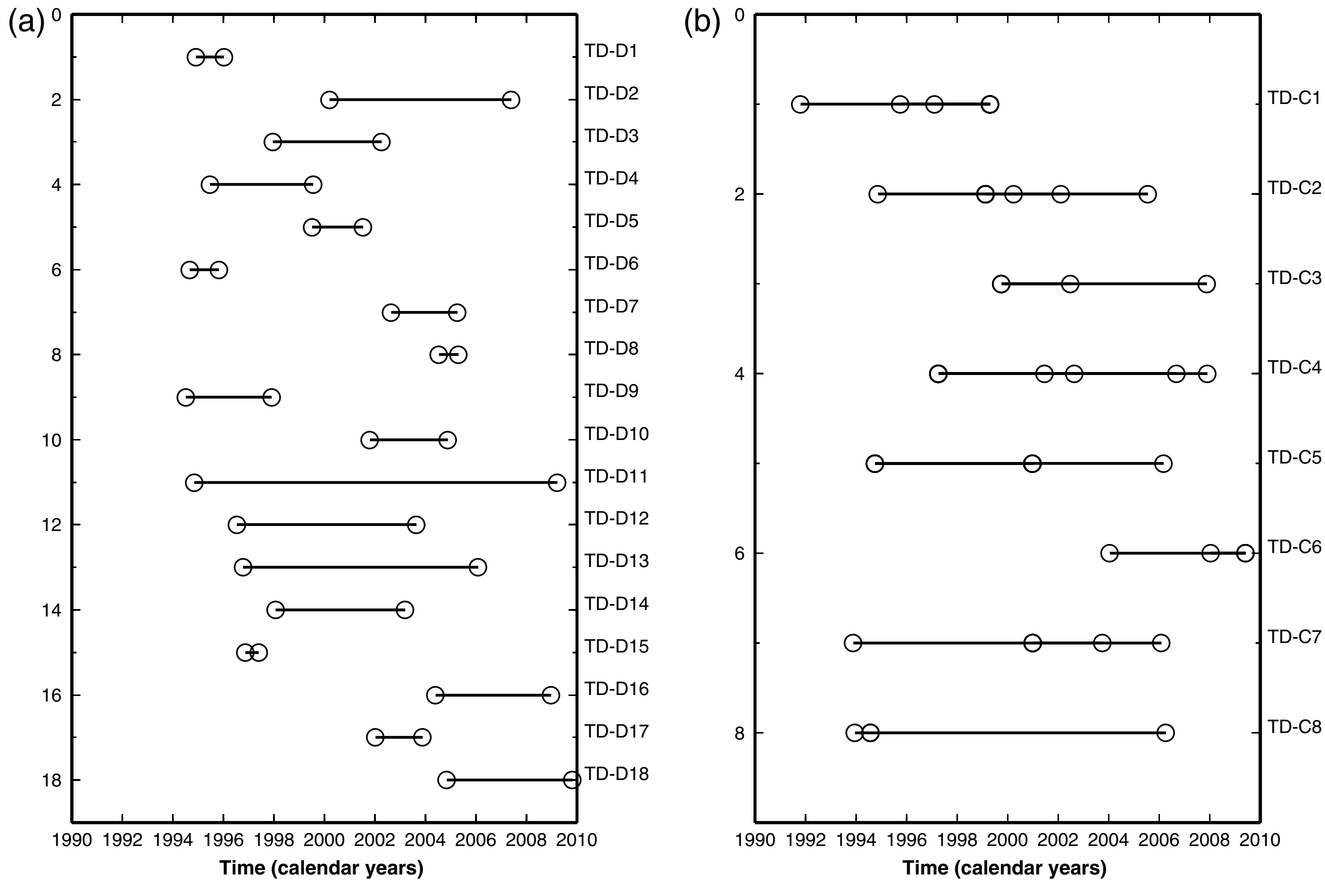

Figure 2. Time window for deep-focus similar (a) doublets and (b) clusters. The abbreviations TD-D and TD-C refer to Tonga deep doublet and Tonga deep cluster, respectively. The digits of the doublet ID and cluster ID increase as latitude of the reference event increases.

at the depth range of 480–650 km (Fig. 1; Tables 1, 2). Time separation is on the order of years for the majority of the earthquake pairs (Fig. 2).

Master Event Algorithm

A master event algorithm (Wen, 2006) is applied to determine the precise relative location and depth between the deep event pairs. This algorithm treats one event of the pair as the master (or reference) event whose origin time and hypocenter are fixed to those of the PDE catalog. The origin time error and relative location and depth of the second event are solved via a grid searching technique. The data are the travel time residuals of the seismic phase pairs calculated by waveform cc of the high-frequency *P* and *PKP* waveform pairs filtered in the frequency range of 0.8–2.0 Hz. The travel time residual is sensitive to the time shift due to differential location and depth and event origin time error between two earthquakes, and it is insensitive to heterogeneous velocity structures along the ray paths because the event pair should be close in space and have nearly identical ray paths. While the absolute location and depth of the master event might be biased by the 3D heterogeneous velocity structures near the source, the relative location between earthquake pairs should be more precise. Event origin time error is treated as a constant and is calculated by averaging the travel time residuals for a given earthquake pair. The optimum location and depth of the second event relative to the master event are solved by grid searching the region near the master event that yields the minimum root mean square (rms) time residual. The box for the grid search is 30 km (east–west) $\times$ 30 km (north–south) $\times$ 30 km (vertical) centered at the hypocenter of the master event (Fig. 3). The interval of grid search is 100 meters in the east–west, north–south, and vertical directions. We use *P*, *PKP* (bc or ab), and *PKKP*bc phases to determine the relative location and depth between earthquake pairs. Surface reflected *pP* phases sampling the upper focal hemisphere are used to improve the precision of relative depth when the phase pair are well recorded. However, surface reflected *pP* phases often cannot be identified simultaneously for both earthquakes due to background noise or unfavorable focal mechanism for the excitation of *pP* phases. To achieve subsample precision, the time series are interpolated to 5 ms sampling rate before cc.

To estimate the location uncertainties, we compute the 95% confidence ellipse for each earthquake pair with 200

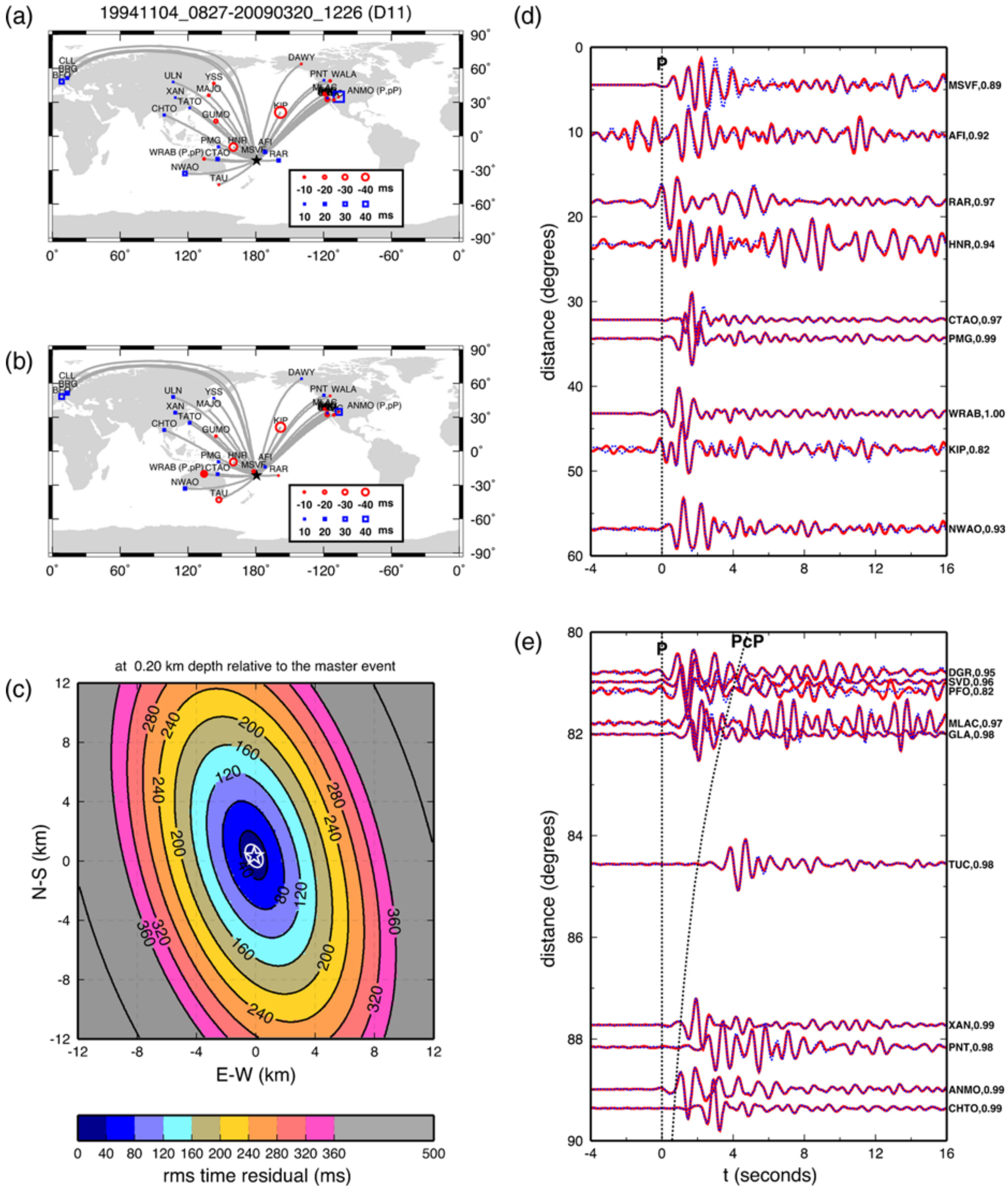

Figure 3. Relocation result and waveforms for the 19941104_0827 (reference event) and 20090320_1226 earthquake pair (D11). *P* and *PKP*bc phases are used to determine the relative location and depth between the event pair. (a) Travel time residuals subtracted from the mean of all travel time residuals (the event origin time error) between the event pair plotted at the location of each seismograph, with the great circles paths (gray traces). (b) Predicted travel time residuals based on the optimum location and depth of the second event relative to the master (reference) event plotted at the location of each seismograph. Negative and positive travel time residuals are indicated by circles and squares, respectively, and the magnitude of the travel time residual is proportional to the size of the symbol. (c) rms time residual near the earthquake source, labeled by black contours and color intensity. Coordinate (0, 0) corresponds to the location of the master event. White open star corresponds to the optimum location and depth of the second event. White open ellipse corresponds to the 95% confidence ellipse calculated with 200 bootstrap resamplings. (d, e) Examples of high-frequency *P* waveforms band-pass filtered in the frequency range of 0.8–2 Hz for the 19941104_0827 (solid traces) and 20090320_1226 (dotted traces) earthquakes with station name and cross-correlation (cc) coefficient shown in the right side of the panel. Waveforms for the reference event are aligned by the predicted *P* arrival of the IASP91 model (Kennett and Engdahl, 1991), whereas waveforms for the second event are aligned by waveform cc between the two traces. The color version of this figure is available only in the electronic edition.

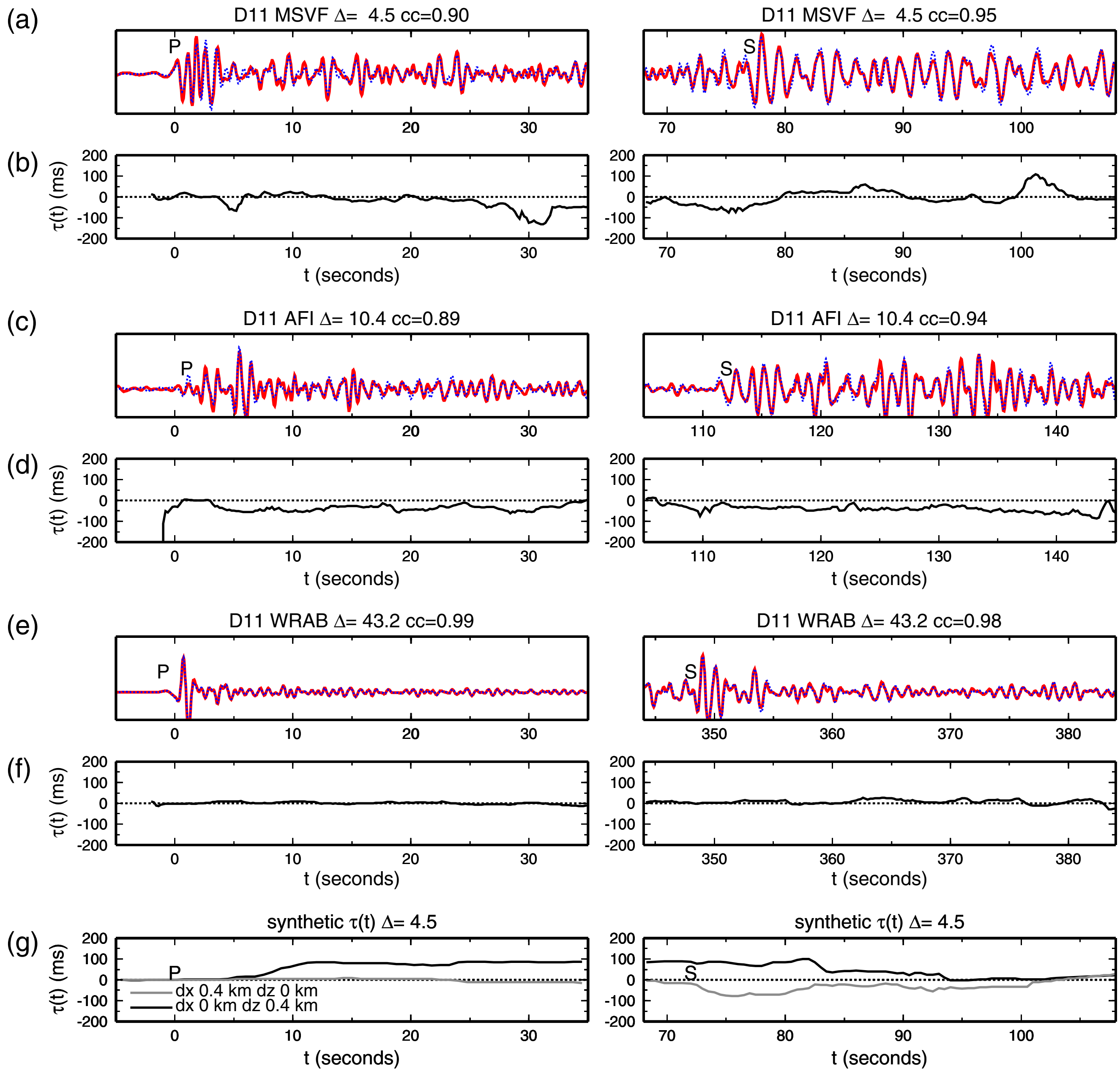

Figure 4. Observed high-frequency (0.8–2 Hz) waveforms and lag time $\tau(t)$ between the D11 doublet and synthetic test for the effect of differential location and differential depth between an earthquake pair. High-frequency *P*-coda (left panels) and *S*-coda (right panels) waveforms in a 40-s time window and their measured lag time series $\tau(t)$ at seismographs (a, b) MSVF, (c, d) AFI, and (e, f) WRAB. Solid traces and dotted traces correspond to the 19941104_0827 (reference event) and 20090320_1226 earthquakes of the D11 doublet, respectively. Station name, epicentral distance, and average waveform cc coefficient of the *P* or *S* coda between the doublet are displayed at the top of the panel. (g) Synthetic $\tau(t)$ due to a lateral separation of 0.4 km (labeled with "dx 0.4 km dz 0 km", gray line) and a vertical separation of 0.4 km (labeled with "dx 0 km dz 0.4 km", black line). Synthetic $\tau(t)$ are calculated from moving window cc between the synthetics based on a focal depth of 600 km and those with a lateral and vertical separation of 0.4 km at the synthetic hypocenter. Note that the vertical separation of 0.4 km produces about 90 ms in lag time near the onset of the *P* coda (black line), which is not observed at MSVF. Note also the observed lag time of the *S* coda at MSVF is generally less than 60 ms, consistent with the synthetic ones of 70 ms based on a horizontal separation of 0.4 km (gray line). The color version of this figure is available only in the electronic edition.

bootstrap resamplings. Eighty percent of the travel time residuals of the seismic phases are randomly selected and used in each bootstrap calculation. The 95% confidence ellipse is estimated using the least squares fit to the 200 locations. Aside from the trade-off between accuracy and computational labor among various methods to determine the location

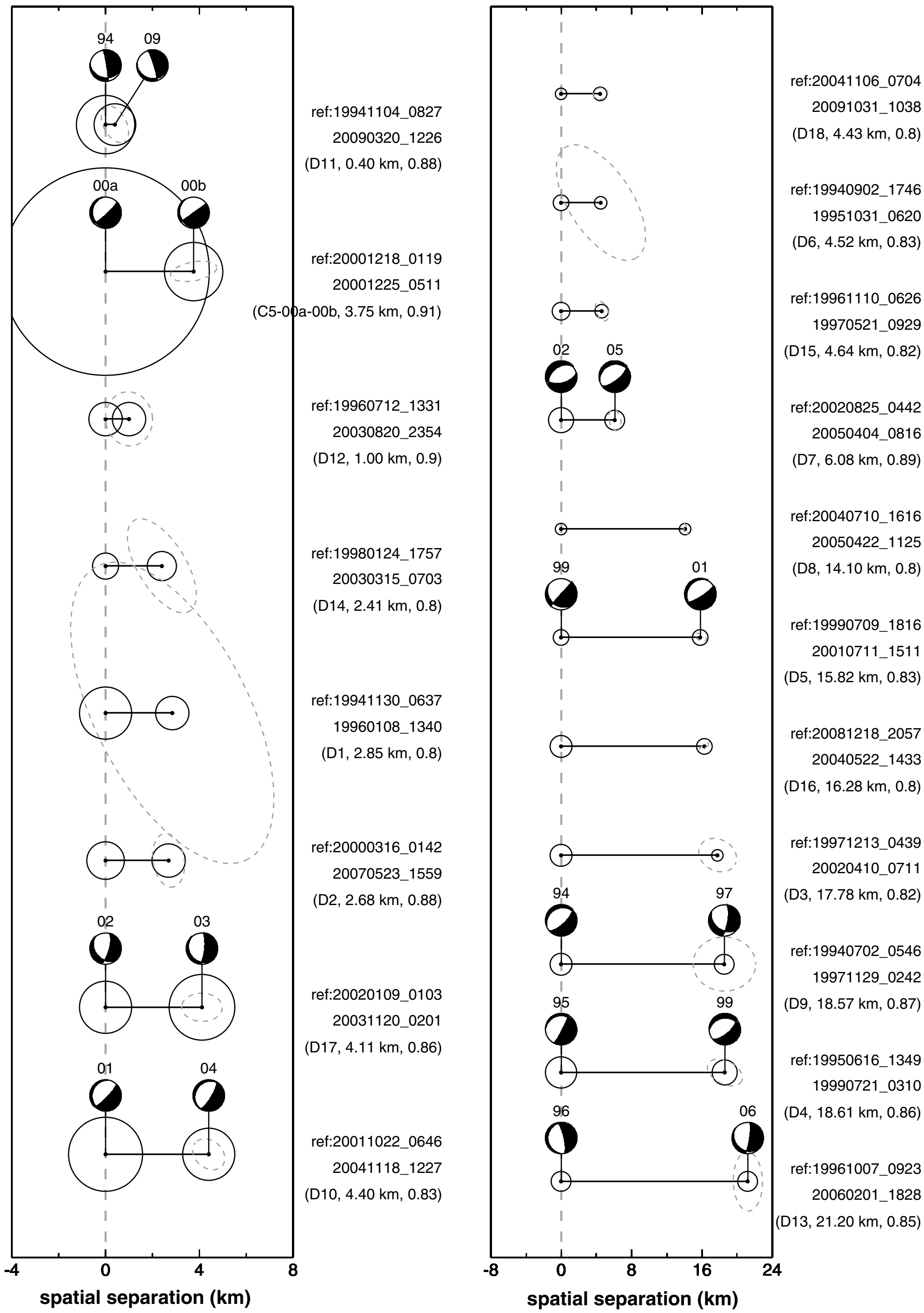

Figure 5. Spatial separation for the 18 deep similar doublets and the C5-00a-00b pair of the cluster C5 in the Tonga–Fiji region. The reference events are placed at 0 km. Black circles refer to the estimated circular source areas, whereas gray dashed ellipses are the location uncertainties of the second event computed from bootstrap resamplings. Size of the circles and ellipses is scaled based on their separation along the *x* coordinate. In the right side of the panel labeled with the reference event ID ("ref" top row), the second event ID (middle row), and the doublet ID, spatial separation in kilometers, and average cc coefficient (bottom row). Two earthquake pairs that have overlap in their fault areas are the D11 and C5-00a-00b pairs. Note that the large difference in source size between the C5-00a-00b pair due to the events 00a and 00b with an m_b 6.4 and 5.3, respectively. The source parameters, precise location, and depth relative to the reference event, time separation, and average *cc* coefficient of the doublets are displayed in Table 1.

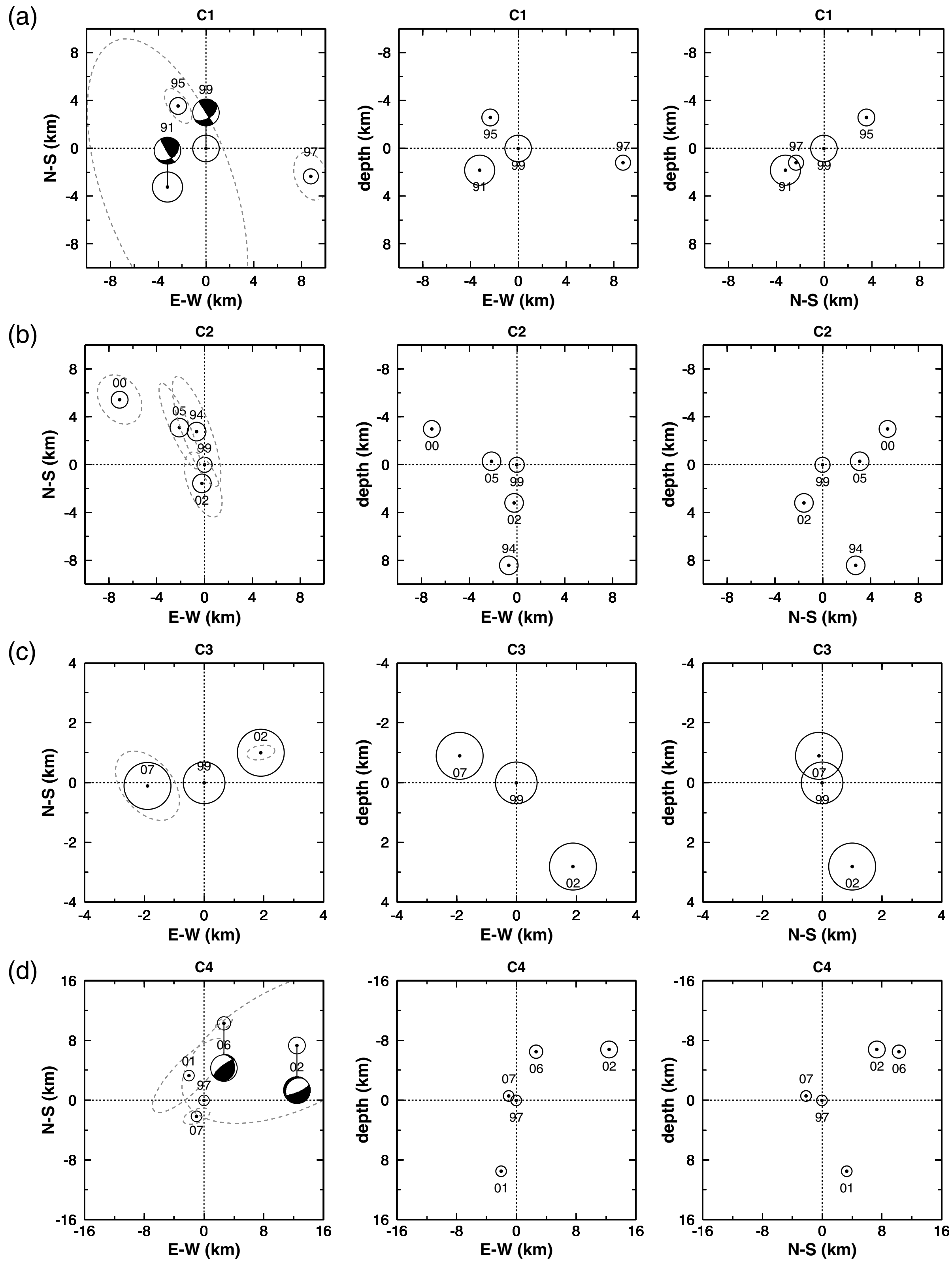

Figure 6. Relative location and depth for the 8 deep similar clusters (a) C1, (b) C2, (c) C3, (d) C4, (e) C5, (f) C6, (g) C7, and (h) C8. Left, middle, and right panels display east–west and north–south plane view, east–west depth plane view, and north–south depth plane view, respectively, among the clusters. Reference events of the clusters are located at coordinate (0, 0). Black circles and gray dashed ellipses refer to the estimated circular source areas and location uncertainties, respectively. Individual earthquakes within each cluster are denoted by year. Only available CMTs are plotted. Note that the estimate of location uncertainties is robust in the east–west north–south plane. Thus, location uncertainties are displayed only in the left panels. The source parameters of the clusters C1–C8 are displayed in Table 2.(*Continued*)

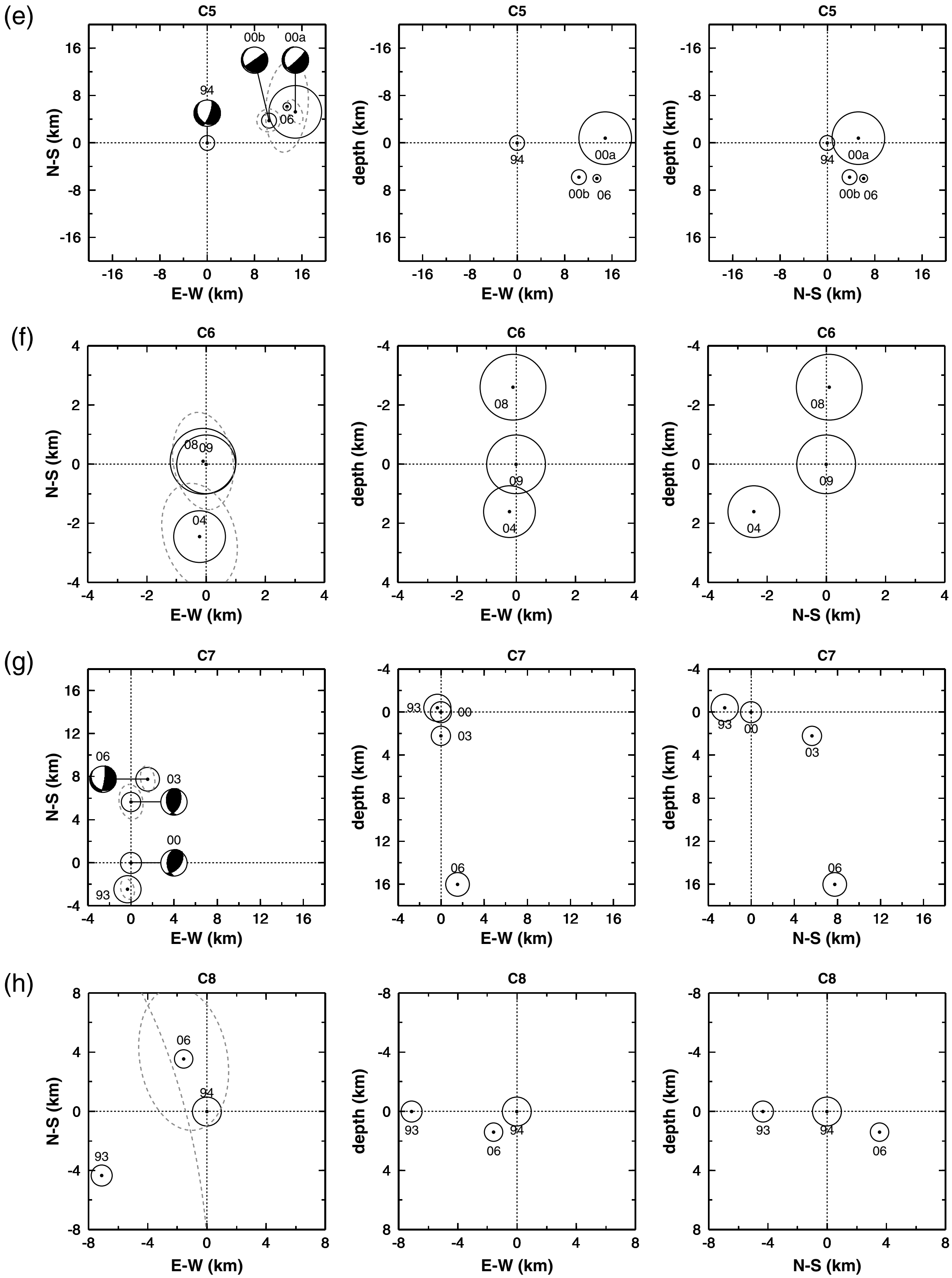

Figure 6. Continued.

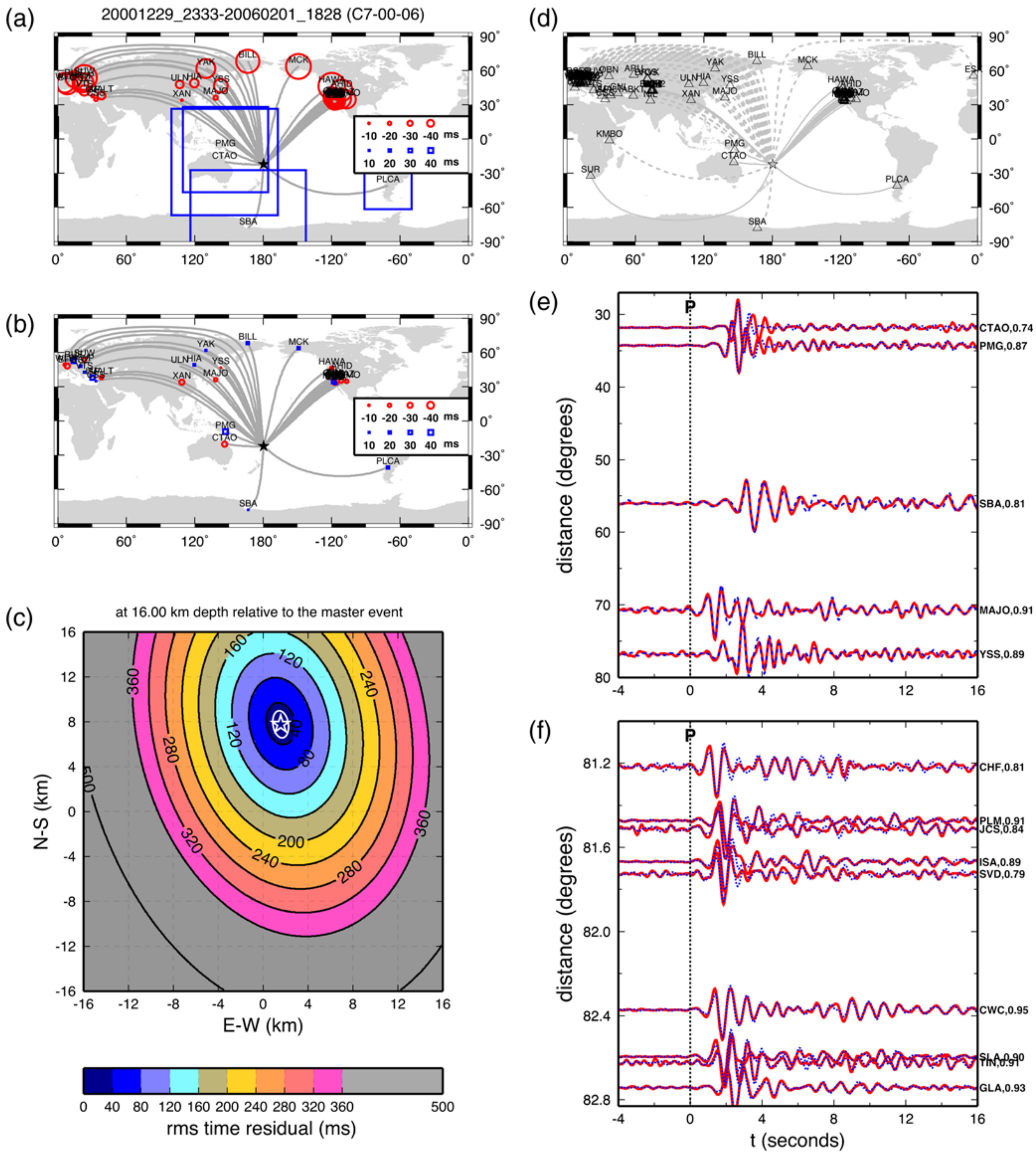

Figure 7. Relocation result and waveforms for the 20001229_2333 (reference event) and 20060201_1828 earthquake pair (C7-00-06 pair) of the cluster C7. (a–c) are same as those in Figure 3. (d) Sampling paths for the display of the phase pairs that have identical polarity (gray solid lines) and reverse polarity (gray dashed lines) between the pair. (e–j) High frequency *P* and *PKP* waveforms band-pass filtered in the frequency range of 0.8–2 Hz at various distance ranges. Solid traces are waveforms of the 20001229_2333 event, whereas dotted traces and dashed traces indicate waveforms of the 20060201_1828 event that have identical and reverse polarity compared with those of the 20001229_2333 event, respectively. Note that waveform cc coefficients of many phase pairs can approach 0.8 after reversing the polarity (solid traces versus dashed traces). Alignment of the waveforms is same as that in Figure 3. Note also the discrepancy in sampling paths between (a) and (d) is that the inner core related phases *PKP*df and *PKiKP* are not included in the relocation displayed in (a). The color version of this figure is available only in the electronic edition. (*Continued*)

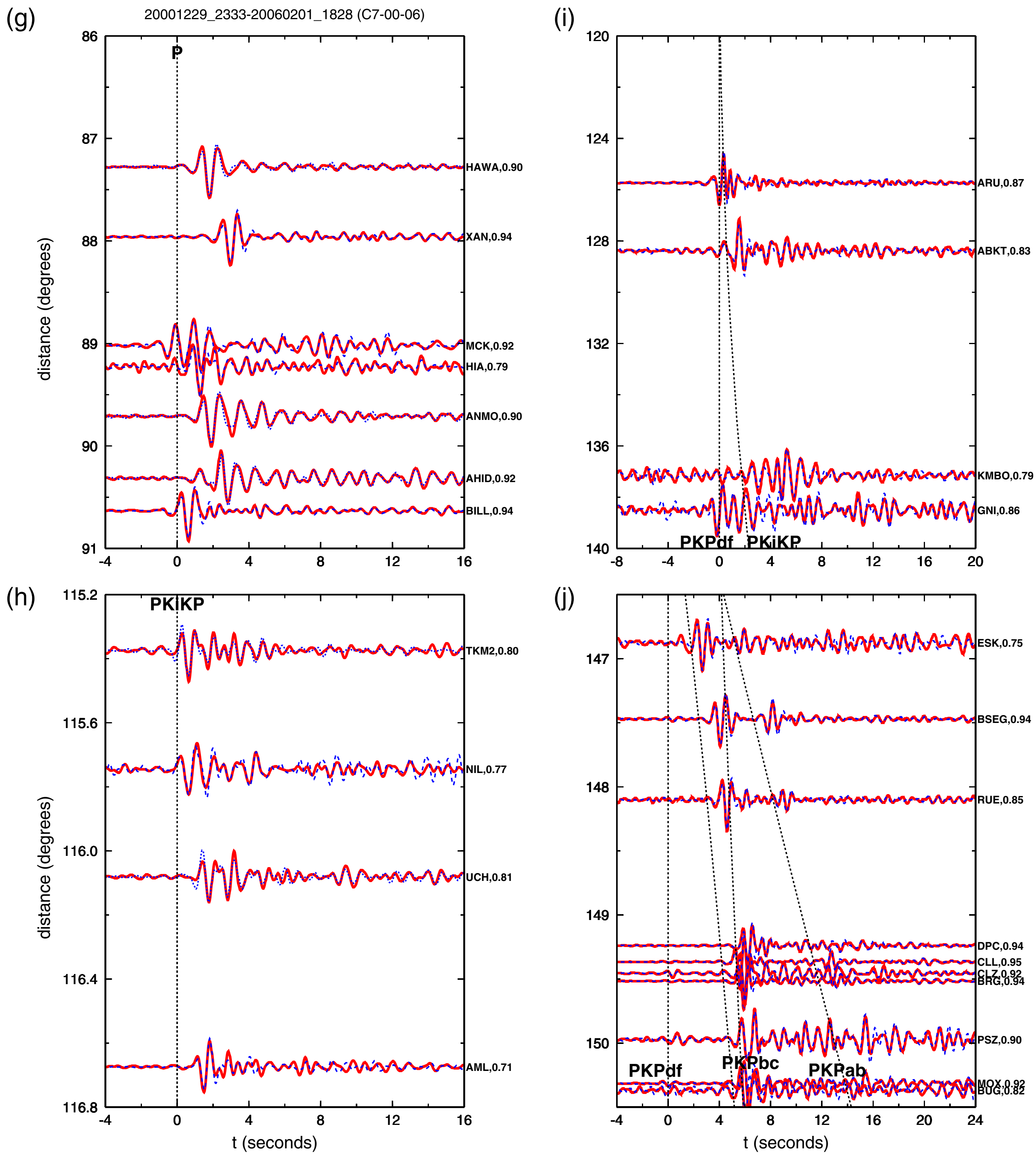

Figure 7. Continued.

uncertainties, precision of the location uncertainties also strongly depends on the sampling coverage and number of measurements. With reasonably good azimuthal coverage, bootstrap resamplings can attain the stability of the location uncertainties (Waldhauser and Ellsworth, 2000), although it is expensive to compute.

Relocation Results and Estimation of the Rupture Zone of an Earthquake

Relocation Results of the D11 Doublet

Our relocation results reveal that the earthquake pair D11, consisting of events 19941104_0827 (m_b 5.3,

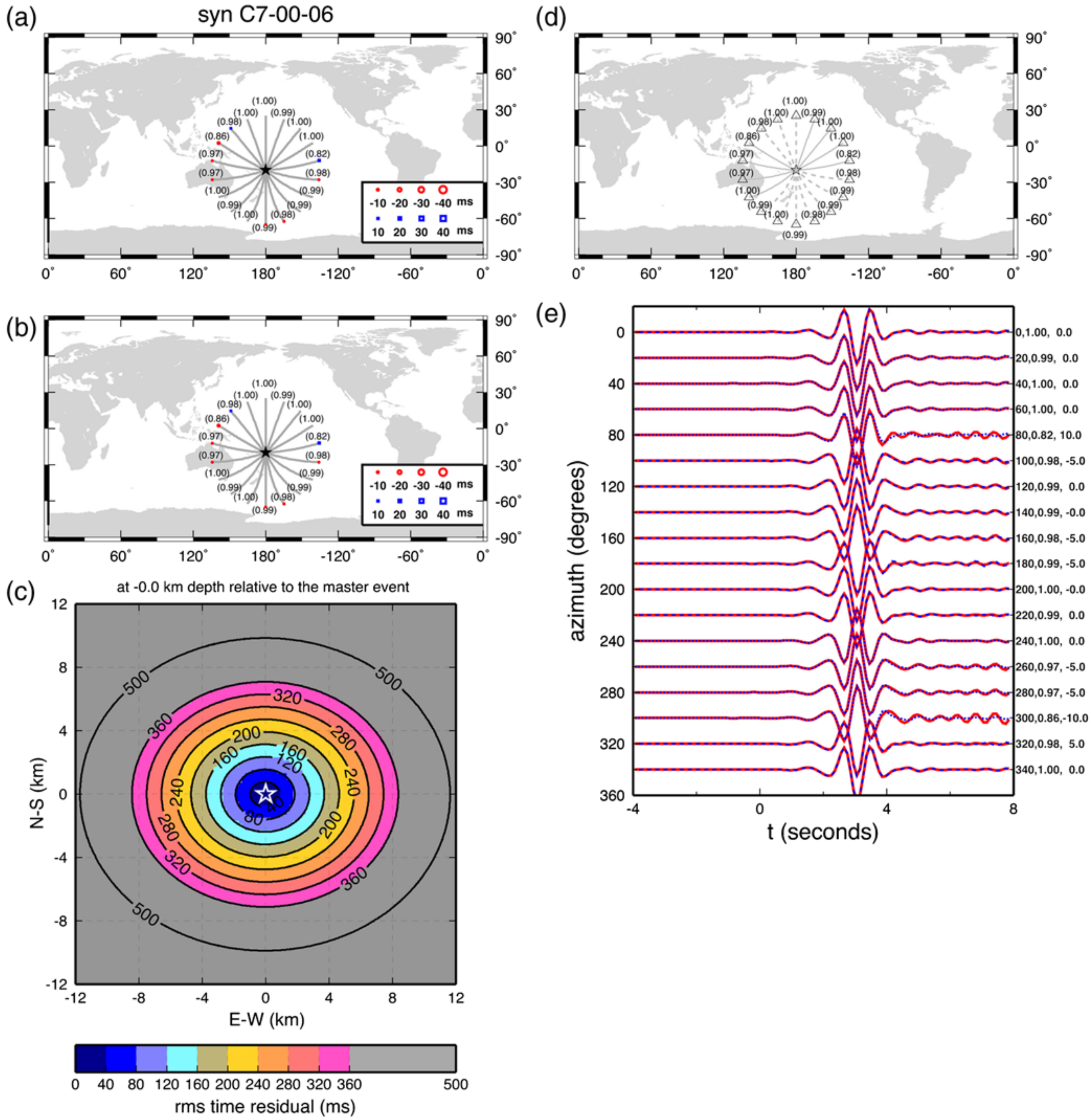

Figure 8. Synthetic relocation result and waveforms based after the 20001229_2333 and 20060201_1828 earthquake pair (syn C7-00-06). We compute two sets of *P*-wave synthetic seismograms using focal mechanism of the 20001229_2333 and 20060201_1828 earthquakes in the Global CMT. Synthetic *P*-wave seismograms are computed at an epicentral distance of 45° and a focal depth of 600 km with azimuth increasing from 0° to 340° with 20° increment. (a–d) are same as those in Figure 7. In (d), cc coefficients are labeled in the parenthesis. (e) Synthetic *P*-wave seismograms filtered in the frequency range of 0.8–2 Hz are aligned by azimuth. Solid traces are the synthetics using focal mechanism of the 20001229_2333 event, whereas dotted traces and dashed traces are the synthetics using focal mechanism of the 20060201_1828 event that have identical and reverse polarity compared with those of the 20001229_2333 event, respectively. In the right side of the panel labeled with azimuth, cc coefficient, and time residual in the unit of millisecond between two traces. Given focal mechanism of the two events in the Global CMT, the unchanged or flipped polarities from the synthetics (d) are similar to the observations (Fig. 7d) to the first order. Note also variations in focal mechanism have negligible effects on the travel time residual and the relocation results (travel time residual of 0 millisecond between solid traces and dashed traces in [e]). The color version of this figure is available only in the electronic edition.

616 km depth) and 20090320_1226 (m_b 5.0, 616.2 km depth), is the spatially closest pair among all deep similar doublets and clusters (Fig. 3). The D11 pair has samplings at stations MSVF and AFI at epicentral distance 4.5° and 10.4°, respectively, and good azimuthal sampling coverage at teleseismic distances (Fig. 3a). The surface reflected *pP* phases at stations WRAB and ANMO are incorporated in the relocation analysis (Fig. 3b), because the *pP* phases can be clearly identified for both events, and their cc coefficients are greater than 0.8. The seismographs in Antarctica did not record both the 1994 and 2009 events. This event pair was recorded by station SPA in 1994 and by station QSPA for the 2009 event; SPA was moved to QSPA (offset by 7.9 km) in 2003–2004. The master event relocation shows that the D11 doublet is separated by 0.35 km and 0.2 km in horizontal and vertical space, respectively (Fig. 3c; Table 1). The major and minor axes of the 95% confidence ellipse are 1.67 km and 1 km, respectively (white ellipse in Fig. 3c; Table 1). Besides the high waveform cc coefficient at all distances and along various sampling azimuth (Fig. 3d,e), the relocation results show that: (1) the travel time residuals subtracted from the average of all travel time residuals (equivalent to the event origin time error of the catalog) (Fig. 3a) are generally similar to those predicted based on the best-fitting location of the second event (Fig. 3b), which simply reflects that the travel time residuals are dominated by the event origin time error; (2) the travel time residuals at the closest stations MSVF and AFI are −13 ms and 11 ms, respectively (Fig. 3b); and (3) the rms time residual predicted based on the optimum location and depth of the second event is 19 ms. The previously stated characteristics inferred from the master event relocation resemble those for shallow-focus repeating earthquakes (Wen, 2006; Yu *et al.* unpublished manuscript, 2012).

Assessment of Differential Location and Differential Depth Using Lag-Time Series

The effect of differential location and differential depth between two earthquakes can also be studied by comparing the lag time series, $\tau(t)$, between observations and synthetics (Niu *et al.*, 2003; Yu *et al.* unpublished manuscript, 2012). For the measurement of the observed $\tau(t)$, we first interpolate the time series of high-frequency waveforms to a sampling rate of 5 ms. A moving window cc of 8 s with a 95% window overlap is used to obtain smooth and stable measurements in delay time of the coda waves between two events. By subtracting the delay time determined solely from cc of the first 4 s of high-frequency *P* wave between two events, we obtain the $\tau(t)$ where t is lapse time (Fig. 4b,d,f). The calculation can be expressed in the form of $(t\text{coda}^2 - t\text{coda}^1) - (tP^2 - tP^1)$. Lag time series in the time window of the *S*-wave coda are equivalent to *S–P* lag time. We compute 2D finite difference synthetic seismograms (Helmberger and Vidale, 1988) based on the preliminary reference Earth model velocity model (Dziewonski and Anderson, 1981) at a focal depth of 600 km and based on the same model with a lateral and vertical separation of 0.4 km at the synthetic hypocenter. Synthetic $\tau(t)$ are computed from moving window cc between two sets of synthetic seismograms (Fig. 4g).

We examine waveform similarity and compare $\tau(t)$ between observations and synthetics with a lateral separation of 0.4 km and a vertical separation of 0.4 km (Fig. 4). The high-frequency *P*- and *S*-coda waveforms recorded at seismographs MSVF, AFI, and WRAB in a 40-s time window between D11 have an average cc coefficient approaching 0.9 and above (Fig. 4a,c,e), and the lag time of the early part of the *S*-wave coda is generally less than 60 ms in absolute value (Fig. 4b,d,f). Similar to the demonstration of Yu *et al.* (unpublished manuscript, 2012), a horizontal separation of 0.4 km between an earthquake pair produces a step increase in the synthetic lag time near the onset of the *S* wave of about 70 ms in absolute value (gray line in Fig. 4g), whereas a vertical separation of 0.4 km produces a step increase in synthetic lag time near the onset of the direct *P* wave of about 90 ms (black line in Fig. 4g). Because the coda waves immediately after the direct *P* wave have a similar vertical slowness as the *P* wave, the difference in depth would have a greater influence on the time delay of the coda waves immediately after the direct *P* wave. On the other hand, the later part of the coda has a similar horizontal slowness as the direct *P* wave and is more sensitive to the effect of differential location. The observed lag time of about 60 ms near the onset of the *S* wave is consistent with the synthetic lag time with a horizontal separation of 0.4 km. Furthermore, the nonobserved step increase in lag time near the onset of the direct *P* wave indicates that the D11 doublet is essentially located at the same focal depth (Fig. 4b,d,g).

Estimating the Circular Rupture Zone of an Earthquake

To determine whether similar earthquake pairs are repeating earthquakes, that is, the earthquake pairs are colocated and their rupture areas overlap, it is essential to estimate the rupture area of an individual earthquake and plot the rupture areas relative to the hypocenter. We use the empirical relationship $M_0 = (16/7)\Delta\sigma a^3$ to estimate the radius of a circular fault (Kanamori and Anderson, 1975), where M_0 is seismic moment, $\Delta\sigma$ is stress drop, and a is the radius of a circular fault. For the 1994 Tonga deep earthquake (M_w 7.6), several seismic studies estimate stress drop to range from 13 to 26 MPa (Wiens, 2001). To be conservative in estimating the fault area, we take an upper bound of 25 MPa to estimate the size of a circular fault for all deep earthquakes in the Tonga–Fiji region. While estimated stress drop can have an uncertainty of a factor of 2, the resultant uncertainty for the estimation of the circular fault is small. For instance, for an m_b 5.2 earthquake, the radius is 1.11 km using $\Delta\sigma$ of 25 MPa. The radius increases to 1.38 km with $\Delta\sigma$ of 13 MPa. The circular fault area increases only by 6% if we decrease $\Delta\sigma$ from 25 MPa to 13 MPa.

Characteristics of Deep-Focus Similar Doublets and Clusters in the Tonga–Fiji Subduction Zone

The source parameters and the estimated circular fault areas for the deep similar doublets and clusters are displayed in Tables 1, 2 and Figures 5, 6. For each similar cluster, we select the reference event as the earthquake that occurred in the late 1990s or in the 2000s with an m_b of about 5.0. Since the deployment of the GSN and other regional seismic networks became more uniform worldwide in the late 1990s, reference events that occurred after this time period can provide more travel time measurements and better azimuthal sampling coverage for the successive events in the cluster. Reference events with an m_b 5.0 enhance the signal-to-noise ratio. Because the Global Centroid Moment Tensor (CMT) is not available for all earthquakes and would yield ambiguous nodal planes, the spatial location of all events relative to the reference event located at (0, 0) is displayed in *X*-*Y* plane view (left panel), *X*-*Z* plane view (middle panel), and *Y*-*Z* plane view (right panel) in Figure 6, with *X* as the east–west direction (E–W), *Y* as the north–south direction (N–S), and *Z* as depth.

The D11 and C5-00a-00b pairs exhibit overlapping rupture areas and are hence defined as repeating earthquakes (first and second pairs in the left panel of Fig. 5). The rupture areas are overlain for the D11 doublet. While the C5-00a-00b pair also shows considerable overlap between the 20001218_0119 (m_b 6.4, labeled as 00a) and 20001225_0511 (m_b 5.3, labeled as 00b) earthquakes of the cluster C5, we find that the C5-00a-00b pair is less robust as a deep repeating earthquake pair compared with the D11 doublet because the C5-00a-00b pair is separated by a horizontal space and a vertical space of 3.46 km and 0.9 km, respectively. Other deep similar doublets and clusters appear to be spatially offset, and their estimated rupture areas do not overlap (Figs. 5 and 6).

The previously stated observations hold even when relative location uncertainties are considered. For the majority of the earthquake pairs with both events occurring after 1995, the uncertainties are less than 5 km (Tables 1, 2). For example, the D11 and C5-00a-00b pairs have uncertainties that are smaller than the radius of the reference event (gray dashed ellipse relative to the black circular rupture area in Fig. 5). For the majority of offset earthquake pairs, the 95% confidence ellipses do not lead to overlapping rupture areas for most deep similar earthquake pairs (Figs. 5 and 6).

There are deep similar doublets and clusters with a high average cc coefficient (>0.85) that are significantly offset. For instance, the D12 pair (third pair in the left panel of Fig. 5) has an average cc coefficient 0.9, but the rupture areas do not overlap. Moreover, a few earthquake pairs, such as the D9, D4, and D13 pairs, are offset by 15 km or more, yet they have average cc coefficients in a range of 0.85–0.87 (right panel of Fig. 5). This observation is inconsistent with observations made for shallow-focus repeating earthquakes that exhibit average cc coefficients greater than 0.85 when rupture areas completely overlap (Schaff and Beroza, 2004; Uchida *et al.*, 2007; Chen *et al.*, 2008). Therefore, a high cc coefficient is often used for the identification of shallow repeating earthquakes. However, for deep earthquake pairs, a high cc coefficient alone does not indicate repeating earthquakes. Deep repeating earthquakes should be defined based on overlapping rupture zones in addition to waveform similarity.

It is interesting to note that the 20001229_2333 (00) and 20060201_1828 (06) earthquake pair (labeled as C7-00-06) of the cluster C7, separated by 7.92 km and 16.00 km in horizontal and vertical space, respectively (Fig. 7c), has different focal mechanisms. Along the azimuthal range of 242°–13°, *P* and *PKP* waveform pairs exhibit polarity reversals (Fig. 7d). We reverse the polarity of the waveforms of the 06 event within that azimuthal range and calculate cc coefficients. The cc coefficients of those phase pairs can approach 0.8 or above and produce an average cc coefficient of 0.84 for 89 measurements (Fig. 7; Table 2). The Global CMT suggests that the 00 event has a focal mechanism $\theta = 182°$, $\delta = 46°$, $\lambda = 63°$, and the 06 event has a focal mechanism $\theta = 8°$, $\delta = 80°$, $\lambda = -74°$. To explore this further, we compute two sets of synthetic seismograms along azimuth from 0° to 340° with an increment of 20° using the focal mechanism of the Global CMT (Fig. 8). The unchanged and flipped polarities based on the Global CMT from the synthetics (Fig. 8d) resemble the observations (Fig. 7d) to the first order, confirming that the difference in focal mechanism between the two earthquakes resolved from the Global CMT should be robust. Surprisingly, the difference in dip of the nodal plane and direction of fault slip occurs in a small volume (1.56 km × 7.78 km × 16 km). In particular, the 137° difference in fault slip between the C7-00-06 pair indicates that the fault slip abruptly changes from oblique thrust to oblique normal.

In summary, deep repeating earthquakes are rare. The D11 doublet appears to be the only deep-focus repeating earthquake pair in our dataset. The observed lag time in the time window of the *S*-wave coda at regional distances matches the synthetic lag times with a horizontal separation of 0.4 km. The nonobserved step increase in lag time near the onset of the direct *P* wave indicates that the D11 doublet is located at the same focal depth. The D11 doublet has similar earthquake magnitudes and a time separation of 14.4 years. Moreover, that the D11 doublet exhibits overlapping rupture areas indicates slip along the same fault. While the C5-00a-00b doublet still shows significant overlap in their rupture areas, the C5-00a-00b doublet result is considered less robust. Many deep similar earthquake pairs with an average cc coefficient above 0.8 are spatially offset. The C7-00-06 event pair exhibits polarity reversals along certain azimuth, but we are able to obtain a high cc coefficient if we reverse one set of waveforms. The polarity reversals result from variations in fault plane dip and a nearly opposite slip direction. Unlike shallow repeating earthquakes, our relocation results suggest that a high cc coefficient alone does not reflect colocation between deep earthquake pairs.

Discussion

Comparison with Previous Studies

Wiens and Snider (2001) discovered several deep repeating earthquake clusters with short time separation using data recorded by a regional seismographic network in the Tonga–Fiji region. Several deep similar earthquakes found in our study also appear in their study: the 19940702_0546 event (m_b 5.3) of the doublet D9, the 19951001_1638 event (m_b 4.9) of the cluster C1, and the 19941109_1441 event (m_b 4.9) of the cluster C2. But several deep repeating earthquakes with magnitude above 4.7 found in their study are not included in our study. The inconsistency in deep repeating earthquakes between the two studies may result from the inconsistent earthquake magnitude among various event catalogs, different datasets, and different frequency ranges used to band-pass filter the waveforms. For instance, the 19950525_1645 and 19951001_1638 events are paired in their cluster 2. But the 19950525_1645 event is not included in this study, because the PDE catalog m_b is 4.6, below our magnitude threshold of 4.7. Wiens and Snider (2001) paired the 19940702_0643 event (m_b 5.1) with the 19940702_0546 event in their cluster 1, but this pair is not found by our screening procedure. We band-pass filter the waveforms recorded by the southwest Pacific seismographic network at regional distances and at teleseismic distances using the frequency range analyzed in their study (0.5– 2 Hz) and our study (0.8–2 Hz) and calculate the average cc coefficient. The average cc coefficient computed at 6 regional stations and 48 teleseismic stations are 0.78 and 0.83, respectively, in the frequency range of 0.5– 2 Hz. But the average cc coefficient calculated at the same regional and teleseismic stations decreases to 0.73 and 0.76, respectively, in the frequency range of 0.8–2 Hz, below our average cc coefficient threshold of 0.8. This suggests that additional deep similar earthquake pairs can be identified if we band-pass filter the waveforms differently. The strength of the Wiens and Snider (2001) study is that they are able to identify deep repeating earthquakes and similar earthquake pairs with smaller magnitudes, and the seismographs at closer distance range greatly improve the precision of relative location among deep earthquake pairs. Our study has the advantage of finding similar earthquake pairs with a longer time separation by exploiting the GSN waveform records.

Uncertainty in Relative Location between an Event Pair due to Variations in Focal Mechanism

Variations in focal mechanism have little influence on the travel time residual, and ultimately, the relocation results. Our procedures for searching for similar earthquake pairs preclude pairing events with large differences in waveforms and/or focal mechanisms. We find that the time error due to small differences in waveforms and focal mechanism is on the order of 1–2 samples of Δt. Thus, the relocation results should not be affected by this small time error. Using the synthetic C7-00-06 pair as an example, most travel time residuals are 0 ms, including those phase pairs with reverse polarity (Fig. 8e). Only synthetics at azimuths of 80° and 300° have a travel time residual of ± 10 ms (2 samples of Δt) due to the numerical noise produced by the synthetics computation (small oscillations after the *P* wave in the solid traces at distance of 80° and 300° in Fig. 8e). Relocation results for the synthetics with different focal mechanisms between the C7-00-06 pair show that the synthetic C7-00-06 pair is colocated (Fig. 8c), suggesting that variations in focal mechanisms do not influence the relocation results.

Possible Interpretations

The phase transformational faulting model predicts that, after the transformation of metastable olivine to spinel, spinel becomes superplastic, and no repeated rupture occurs at the same spinel-filled anticracks (Green and Burnley, 1989). The presence of deep repeating earthquakes is not compatible with the prediction of the transformational faulting model.

The thermal (plastic) shear instability model can explain temporal and spatial separation of deep similar earthquake pairs and repeating earthquakes. Thermal conductive cooling and temperature-sensitive rheology are proposed to explain the repeating earthquakes with short time separation on the order of days (Wiens and Snider, 2001). To account for longer time separation on the order of years, strain heating due to internal deformation of the descending slab is likely to lower viscosity and allow shear instability to develop. Deep-focus repeating earthquakes are rare compared with shallow-focus repeating earthquakes, probably due to the fact that deep earthquakes have higher stress drop (13 MPa and above) compared with shallow-focus interplate earthquakes (1 MPa) (Kanamori and Anderson, 1975). This may explain why the successive deep earthquakes occur in the adjacent areas of their preceding events. On the other hand, the presence of deep repeating earthquakes does not indicate lower stress drop. The close proximity of events may be explained by the localized high strain and the associated strain heating, which in turn facilitates thermal shear instability and produces deep repeating earthquakes in certain regions.

Conclusion

We search for deep-focus similar earthquake pairs in the Tonga–Fiji–Kermadec subduction zone using waveforms recorded by the GSN and other regional seismic networks between 1990 and 2009. We find a total of 8 deep-focus similar clusters and 18 similar doublets with an average cc coefficient above 0.8 among more than 45,000 event pairs. These similar clusters and doublets are located in the central part of the Tonga–Fiji slab at the depth range of 480–650 km. Our analyses reveal that the D11 doublet satisfies the definition of repeating earthquakes in that the closeness, overlapping rupture areas, and similarity in earthquake magnitude for D11 are similar to those for shallow-focus repeating earthquakes. Other similar clusters and doublets are spatially offset or do not have considerable overlapping rupture areas. Time separation is on the order of years for the majority of similar earthquake pairs. Thermal (plastic) shear instability more likely explains the presence of deep repeating earthquakes relative to other models proposed to explain deep earthquake occurrence. To account for the wide range of time separation (days to years), temperature-sensitive rheology, thermal conductive cooling, and strain heating from internal deformation of the slab jointly play important roles to reactivate faults or weaken adjacent areas along a shear zone.

Data and Resources

Our seismic data include: the Global Seismographic Network (GSN); the Global Telemetered Seismograph Network (GT); the GEOSCOPE (G); the new China Digital Seismograph Network (CD, IC); the Kazakhstan Seismic Network (KZ); the Kyrgyz Seismic Telemetry Network (KN); the Pacific 21 Seismic Network (PS); XB 1993–1995, XP 2000–2003, YI 1998–2001, and YC 2000–2002 from the Incorporated Research Institutions for Seismology Consortium Data Management Center (IRIS-DMC) (http://www.iris.edu/hq/); the German regional seismic network (GRSN) and Grafenberg seismic network (GRF) from the SZGRF (http://www.szgrf.bgr.de/); and the Canadian National Seismographic Network (CNSN) (http://earthquakescanada.nrcan.gc.ca/stnsdata/wf_index-eng.php). Earthquake focal mechanisms are obtained from the Global Centroid Moment Tensor Project (www.globalcmt.org/CMTsearch.html). Figures were prepared with the Generic Mapping Tools software (Wessel and Smith, 1998) available at http://www.soest.hawaii.edu/gmt/. All the cited web links were last accessed in February 2012.

Acknowledgments

W. Yu thanks Un Joe and Anh Ngo of the IRIS-DMC and Klaus Stammler of the SZGRF for access to the waveforms. Thoughtful suggestions from the associate editor Heather DeShon and two anonymous reviewers greatly improved the presentation of the paper. W. Yu benefited from discussions with Jiuhua Chen, David James, Alan Linde, Laetitia Mozziconacci, Selwyn Sacks, Paul Silver, Sean Solomon, Teh-Ru Alex Song, Linda Warren, and Don Weidner. This study is partially supported by Department of Terrestrial Magnetism, Carnegie Institution of Washington, U.S.A.; Institute of Earth Sciences, Academia Sinica, Taiwan; and the National Science Council grants NSC- 99-2116-M-001-003- and NSC-100-2119-M-001-018-, Taiwan. The TEC contribution number is 00079.

References

Beck, S. L., P. Silver, T. C. Wallace, and D. James (1995). Directivity analysis of the deep Bolivian earthquake of June 9, 1994, *Geophys. Res. Lett.* **22,** 2257–2260.

Bevis, M., F. W. Taylor, B. E. Schutz, J. Recy, B. L. Isacks, S. Helu, R. Singh, E. Kendrick, J. Stowell, B. Taylor, and S. Calmant (1995). Geodetic observations of very rapid convergence and back-arc extension at the Tonga arc, *Nature* **374,** 249–251.

Bird, P. (2003). An updated digital model of plate boundaries, *Geochem. Geophys. Geosyst.* **4**, doi 10.1029/2001GC000252.

Chen, W. P. (1995). En-echelon ruptures during the great Bolivian earthquake of 1994, *Geophys. Res. Lett.* **22,** 2261–2264.

Chen, W. P., and M. R. Brudzinski (2001). Evidence for a large-scale remnant of subducted lithosphere beneath Fiji, *Science* **292,** 2475–2479.

Chen, K. H., R. M. Nadeau, and R. J. Rau (2008). Characteristic repeating earthquakes in an arc-continent collision boundary zone: The Chihshang fault of eastern Taiwan, *Earth Planet. Sci. Lett.* **276,** 262–272, doi 10.1016/J.Epsl.2008.09.021.

Chen, W. P., L. R. Wu, and M. A. Glennon (1996). Characteristics of multiple ruptures during large deep-focus earthquakes, in *Subduction: Top to Bottom*, E. Bebout, W. Scholl, H. Kirby, and P. Platt (Editors), American Geophysical Union, Washington, D.C., 357–368.

Christova, C., and C. H. Scholz (2003). Stresses in the Vanuatu subducting slab: A test of two hypotheses, *Geophys. Res. Lett.* **30**, doi 10.1029/2003GL017701.

Dziewonski, A. M., and D. L. Anderson (1981). Preliminary reference Earth model, *Phys. Earth Planet. In.* **25,** 297–356.

Dziewonski, A. M., T. A. Chou, and J. H. Woodhouse (1981). Determination of earthquake source parameters from waveform data for studies of global and regional seismicity, *J. Geophys. Res.* **86,** 2825–2852.

Ekstrom, G., A. M. Dziewonski, N. N. Maternovskaya, and M. Nettles (2003). Global seismicity of 2001: Centroid-moment tensor solutions for 961 earthquakes, *Phys. Earth Planet. In.* **136,** 165–185, doi 10.1016/S0031-9201(03)00030-X.

Engdahl, E. R., R. van der Hilst, and R. Buland (1998). Global teleseismic earthquake relocation with improved travel times and procedures for depth determination, *Bull. Seismol. Soc. Am.* **88,** 722–743.

Frohlich, C. (1987). Aftershocks and temporal clustering of deep earthquakes, *J. Geophys. Res.* **92,** 13944–13956.

Frohlich, C. (1989). The nature of deep-focus earthquakes, *Annu. Rev. Earth Planet. Sci.* **17,** 227–254.

Frohlich, C. (2006). *Deep Earthquakes*, Cambridge University Press, New York, 573 pp.

Giardini, D., and J. H. Woodhouse (1984). Deep seismicity and modes of deformation in Tonga subduction zone, *Nature* **307,** 505–509.

Giardini, D., and J. H. Woodhouse (1986). Horizontal shear-flow in the mantle beneath the Tonga arc, *Nature* **319,** 551–555.

Green, H. W., and P. C. Burnley (1989). A new self-organizing mechanism for deep-focus earthquakes, *Nature* **341,** 733–737.

Green, H. W., and H. Houston (1995). The mechanics of deep earthquakes, *Annu. Rev. Earth Planet. Sci.* **23,** 169–213.

Green, H. W., T. E. Young, D. Walker, and C. H. Scholz (1990). Anticrack-associated faulting at very high-pressure in natural olivine, *Nature* **348,** 720–722.

Gudmundsson, O., and M. Sambridge (1998). A regionalized upper mantle (RUM) seismic model, *J. Geophys. Res.* **103,** 7121–7136.

Hasegawa, A., N. Umino, and A. Takagi (1978). Double-planed structure of deep seismic zone in northeastern Japan arc, *Tectonophysics* **47,** 43–58.

Helmberger, D. V., and J. E. Vidale (1988). Modeling strong motions produced by earthquakes with two-dimensional numerical codes, *Bull. Seismol. Soc. Am.* **78,** 109–121.

Hobbs, B. E., and A. Ord (1988). Plastic instabilities: Implications for the origin of intermediate and deep-focus earthquakes, *J. Geophys. Res.* **93,** 10521–10540.

Holt, W. E. (1995). Flow-fields within the Tonga slab determined from the moment tensors of deep earthquakes, *Geophys. Res. Lett.* **22,** 989–992.

Houston, H. (2007). Deep earthquakes, in *Treatise on Geophysics 4: Earthquake Seismology*, G. Schubert and H. Kanamori (Editors), Elsevier, Amsterdam, 321–350.

Isacks, B., and P. Molnar (1969). Mantle earthquake mechanisms and sinking of lithosphere, *Nature* **223,** 1121–1124.

Isacks, B., and P. Molnar (1971). Distribution of stresses in descending lithosphere from a global survey of focal-mechanism solutions of mantle earthquakes, *Rev. Geophys. Space Phys.* **9,** 103–174.

Jiao, W. J., P. G. Silver, Y. W. Fei, and C. T. Prewitt (2000). Do intermediate- and deep-focus earthquakes occur on preexisting weak zones? An examination of the Tonga subduction zone, *J. Geophys. Res.* **105,** 28125–28138.

Jung, H., H. W. Green, and L. F. Dobrzhinetskaya (2004). Intermediate-depth earthquake faulting by dehydration embrittlement with negative volume change, *Nature* **428,** 545–549, doi 10.1038/nature02412.

Kanamori, H., and D. L. Anderson (1975). Theoretical basis of some empirical relations in seismology, *Bull. Seismol. Soc. Am.* **65,** 1073–1095.

Kanamori, H., D. L. Anderson, and T. H. Heaton (1998). Frictional melting during the rupture of the 1994 Bolivian earthquake, *Science* **279,** 839–842.

Karato, S., M. R. Riedel, and D. A. Yuen (2001). Rheological structure and deformation of subducted slabs in the mantle transition zone: Implications for mantle circulation and deep earthquakes, *Phys. Earth Planet. In..* **127,** 83–108.

Kawakatsu, H. (1985). Double seismic zone in Tonga, *Nature* **316,** 53–55.

Kennett, B. L. N., and E. R. Engdahl (1991). Travel times for global earthquake location and phase identification, *Geophys. J. Int.* **105,** 429–465.

Kikuchi, M., and H. Kanamori (1994). The mechanism of the deep Bolivia earthquake of June 9, 1994, *Geophys. Res. Lett.* **21,** 2341–2344.

Kirby, S. H., S. Stein, E. A. Okal, and D. C. Rubie (1996). Metastable mantle phase transformations and deep earthquakes in subducting oceanic lithosphere, *Rev. Geophys.* **34,** 261–306.

McGuire, J. J., D. A. Wiens, P. J. Shore, and M. G. Bevis (1997). The March 9, 1994 (M_w 7.6), deep Tonga earthquake: Rupture outside the seismically active slab, *J. Geophys. Res.* **102,** 15163–15182.

Meade, C., and R. Jeanloz (1991). Deep-focus earthquakes and recycling of water into the Earth's mantle, *Science* **252,** 68–72.

Myers, S. C., T. C. Wallace, S. L. Beck, P. G. Silver, G. Zandt, J. Vandecar, and E. Minaya (1995). Implications of spatial and temporal development of the aftershock sequence for the M_w 8.3 June 9, 1994 deep Bolivian earthquake, *Geophys. Res. Lett.* **22,** 2269–2272.

Niu, F. L., P. G. Silver, R. M. Nadeau, and T. V. McEvilly (2003). Migration of seismic scatterers associated with the 1993 Parkfield aseismic transient event, *Nature* **426,** 544–548, doi 10.1038/nature02151.

Ogawa, M. (1987). Shear instability in a viscoelastic material as the cause of deep-focus earthquakes, *J. Geophys. Res.* **92,** 13801–13810.

Schaff, D. P., and G. C. Beroza (2004). Coseismic and postseismic velocity changes measured by repeating earthquakes, *J. Geophys. Res.* **109**, doi 10.1029/2004JB003011.

Silver, P. G., S. L. Beck, T. C. Wallace, C. Meade, S. C. Myers, D. E. James, and R. Kuehnel (1995). Rupture characteristics of the deep Bolivian earthquake of 9 June 1994 and the mechanism of deep-focus earthquakes, *Science* **268,** 69–73.

Uchida, N., T. Matsuzawa, W. L. Ellsworth, K. Imanishi, T. Okada, and A. Hasegawa (2007). Source parameters of a *M* 4.8 and its accompanying repeating earthquakes off Kamaishi, NE Japan: Implications for the hierarchical structure of asperities and earthquake cycle, *Geophys. Res. Lett.* **34**, doi 10.1029/2007GL031263.

Waldhauser, F., and W. L. Ellsworth (2000). A double-difference earthquake location algorithm: Method and application to the northern Hayward fault, California, *Bull. Seismol. Soc. Am.* **90,** 1353–1368.

Warren, L. M., and P. G. Silver (2006). Measurement of differential rupture durations as constraints on the source finiteness of deep-focus earthquakes, *J. Geophys. Res.* **111**, doi 10.1029/2005JB004001.

Warren, L. M., A. N. Hughes, and P. G. Silver (2007). Earthquake mechanics and deformation in the Tonga-Kermadec subduction zone from fault plane orientations of intermediate- and deep-focus earthquakes, *J. Geophys. Res.* **112**, doi 10.1029/2006JB004677.

Warren, L. M., M. A. Langstaff, and P. G. Silver (2008). Fault plane orientations of intermediate-depth earthquakes in the Middle America Trench, *J. Geophys. Res.* **113**, doi 10.1029/2007JB005028.

Weidner, D. J., J. H. Chen, Y. Q. Xu, Y. J. Wu, M. T. Vaughan, and L. Li (2001). Subduction zone rheology, *Phys. Earth Planet. In..* **127,** 67–81.

Wen, L. (2006). Localized temporal change of the Earth's inner core boundary, *Science* **314,** 967–970, doi 10.1126/science.1131692.

Wessel, P., and W. H. F. Smith (1998). New, improved version of the Generic Mapping Tools released, *Eos Trans. AGU* **79,** 579.

Wiens, D. A. (2001). Seismological constraints on the mechanism of deep earthquakes: Temperature dependence of deep earthquake source properties, *Phys. Earth Planet. In.* **127,** 145–163.

Wiens, D. A., and J. J. McGuire (2000). Aftershocks of the March 9, 1994, Tonga earthquake: The strongest known deep aftershock sequence, *J. Geophys. Res.* **105,** 19067–19083.

Wiens, D. A., and N. O. Snider (2001). Repeating deep earthquakes: Evidence for fault reactivation at great depth, *Science* **293,** 1463–1466.

Wiens, D. A., H. J. Gilbert, B. Hicks, M. E. Wysession, and P. J. Shore (1997). Aftershock sequences of moderate-sized intermediate and deep earthquakes in the Tonga subduction zone, *Geophys. Res. Lett.* **24,** 2059–2062.

Wiens, D. A., J. J. McGuire, P. J. Shore, M. G. Bevis, K. Draunidalo, G. Prasad, and S. P. Helu (1994). A deep earthquake aftershock sequence and implications for the rupture mechanism of deep earthquakes, *Nature* **372,** 540–543.

Willemann, R. J., and C. Frohlich (1987). Spatial patterns of aftershocks of deep-focus earthquakes, *J. Geophys. Res.* **92,** 13927–13943.

Zhang, J. F., H. W. Green, K. Bozhilov, and Z. M. Jin (2004). Faulting induced by precipitation of water at grain boundaries in hot subducting oceanic crust, *Nature* **428,** 633–636, doi 10.1038/Nature02475.

Institute of Earth Sciences
Academia Sinica
No. 128 Section 2, Academia Road
Nangang, Taipei, 11529, Taiwan
fgsyw@earth.sinica.edu.tw
(W.Y.)

Department of Geosciences
State University of New York at Stony Brook
Stony Brook, New York 11794-2100
lwen@notes.cc.sunysb.edu
(L.W.)

Manuscript received 28 September 2011